

# Dramatically Enhanced Broadband Photodetection by Dual Inversion Layers and Fowler–Nordheim Tunneling

Haiyang Zou,<sup>†</sup> Xiaogan Li,<sup>†</sup> Guozhang Dai,<sup>†,‡</sup> Wenbo Peng,<sup>†</sup> Yong Ding,<sup>†</sup> Ying Zhang,<sup>†</sup> Aurelia Chi Wang,<sup>†</sup> Steven L. Zhang,<sup>†</sup> Cheng Xu,<sup>†,§</sup> Shi-Li Zhang,<sup>\*,||</sup> and Zhong Lin Wang<sup>\*,†,||,⊥</sup>

<sup>†</sup>School of Materials Science and Engineering, Georgia Institute of Technology, Atlanta, Georgia 30332-0245, United States

<sup>‡</sup>Hunan Key Laboratory for Super-microstructure and Ultrafast Process, School of Physics and Electronics, Central South University, Changsha, Hunan 410083, People's Republic of China

<sup>§</sup>School of Materials Science and Engineering, China University of Mining and Technology, Xuzhou 221116, People's Republic of China

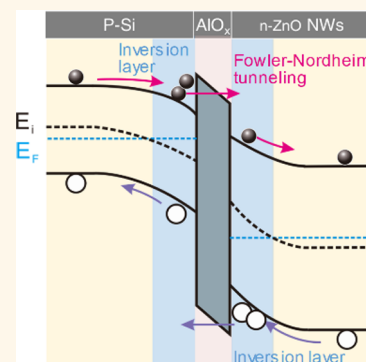
<sup>||</sup>Solid-State Electronics, The Ångström Laboratory, Uppsala University, SE-751 21, Uppsala, Sweden

<sup>⊥</sup>Beijing Institute of Nanoenergy and Nanosystems, Chinese Academy of Sciences, Beijing 100083, People's Republic of China

## Supporting Information

**ABSTRACT:** Silicon photonics is now widely accepted as a key technology in a variety of systems. But owing to material limitations, now it is challenging to greatly improve the performance after decades of development. Here, we show a high-performance broadband photodetector with significantly enhanced sensitivity and responsivity operating over a wide wavelength range of light from near-ultraviolet to near-infrared at low power consumption. The specially designed textured top ceiling electrode works effectively as an antireflection layer to greatly improve the absorption of near-infrared light, thereby overcoming the absorption limitation of near-infrared light. Instead of the conventional p–n junction and p–intrinsic–n junction, we introduce a ~15 nm thick alumina insulator layer between a p-type Si substrate and n-type ZnO nanowire (NW) arrays, which significantly enhances the charge carrier separation and collection efficiency. The photosensing responsivity and sensitivity are found to be nearly 1 order of magnitude higher than that of a reference device of p-Si/n-ZnO NW arrays, significantly higher than the commercial silicon photodiodes as well. The light-induced charge carriers flow across the appropriate thickness of insulator layer *via* the quantum mechanical Fowler–Nordheim tunneling mechanism. By virtue of the piezo-phototronic effect, the charge density at the interfaces can be tuned to alter the energy bands and the potential barrier distance for tunneling. Additionally, along with the use of incident light of different wavelengths, the influence of the insulator layer on the transport of electrons and holes separately is further investigated. The demonstrated concepts and study would lead to sensitivity improvement, quality enhancement of data transfer, decrease of power consumption, and cost reduction of silicon photonics.

**KEYWORDS:** broadband photodetectors, piezo-phototronic effect, inversion layer, Fowler–Nordheim tunneling, p–insulator–n junction, atomic layer deposition, alumina



Silicon photonics has been revolutionizing many application areas vital for modern society, including communication systems, computing, biomedical diagnostics, imaging, and sensing.<sup>1–4</sup> Silicon does, however, have a number of shortcomings as a photonic material.<sup>5</sup> Its indirect energy band and highly reflective surface limit the absorption of light,<sup>6,7</sup> especially the near-infrared light (NIR) above 900 nm.<sup>1,8,9</sup> When the incident optical power increases, the silicon photonic devices will reach a saturation limit<sup>10</sup> and the responsivity falls significantly due to various optical loss mechanisms (such as reflection, heat, incomplete absorption,

and indirect bandgap) and recombination of photoinduced carriers.<sup>11–13</sup> In current photodiodes, doping at high temperature to form a p–n junction is popular, but this process is costly, consumes energy, and requires extra care of cleanliness; furthermore, in highly doped regions, doping-induced crystal damage and/or Auger recombination limit further improvement of light response in these photodiodes.<sup>14</sup> To reduce the

**Received:** November 27, 2018

**Accepted:** January 24, 2019

**Published:** January 24, 2019

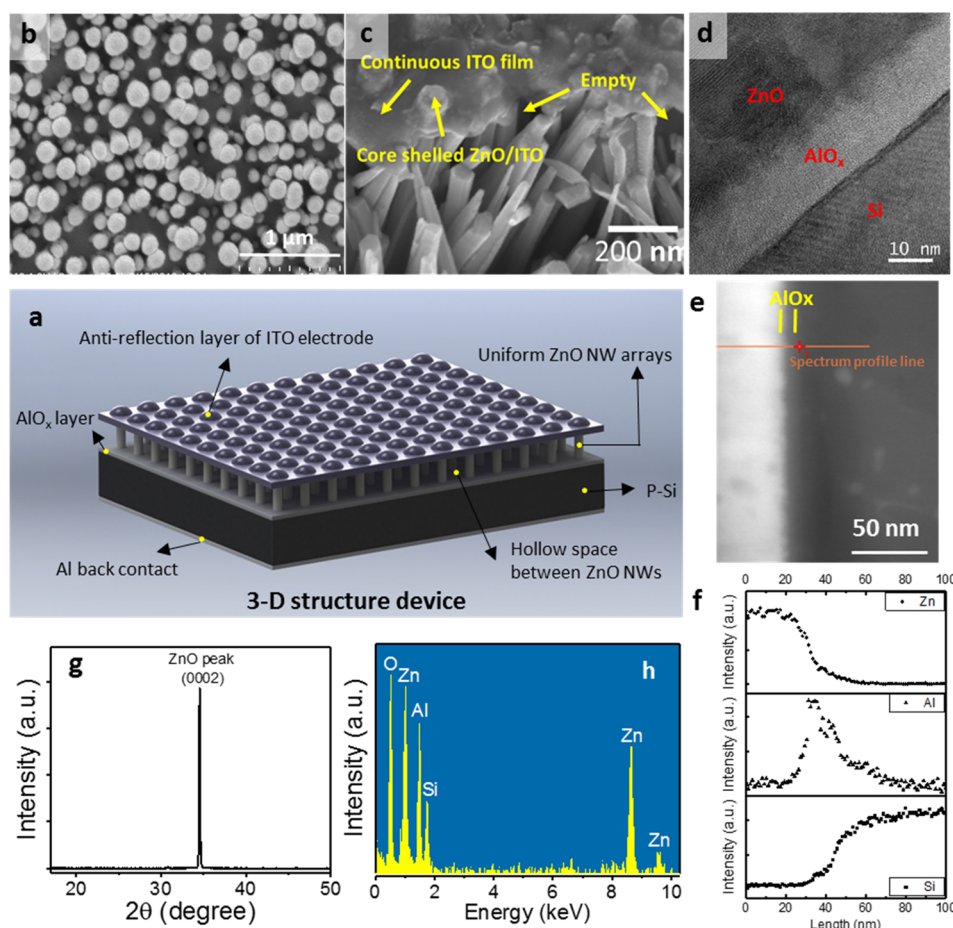


**Figure 1.** Device fabrication and structural characterization. (a) Schematic of a 3D structure of a p-Si/AIO<sub>x</sub>/n-ZnO NW array photodetector. A thin film of insulator AlO<sub>x</sub> is deposited on the p-Si substrate. The nanowire arrays were grown vertically on the insulator layer. The ITO layer was core–shelled with the tips of ZnO nanowires, suspended as the ceiling. (b, c) SEM images of the top surface view of the device and 30° side view of the top surface of the ITO coating at the edge of the device, respectively. The ceiling top electrode has an enokitake mushroom-like texture nanostructure. (d) TEM images of the cross-section. The red line in (e) is the scanning route of the spectrum profile. (f) Spectrum profile of the cross-section. (g) X-ray diffraction of ZnO nanowires on Si. (h) Energy dispersive X-ray spectroscopy spectrum of the device.

front surface reflectance of a planar surface, conventional antireflection coatings with different thicknesses and refractive indices are effective.<sup>15–17</sup> This approach could result in improved sensitivity in a certain wavelength range; however, it may reduce responsivity at other wavelengths and increase the cost.<sup>14,15,18</sup> Developing nanostructures in the devices can improve the light response by providing longer optical paths, wider acceptance angles, and low surface reflection, but its large effective surface area significantly increases recombination at the device surface.<sup>14</sup> The hybrid integration of III–V materials onto silicon to improve the NIR light absorption is yet to become cost-effective.<sup>1,19</sup> Overall, to offer the lowest possible power consumption while significantly improving the performance of silicon photonics in terms of high responsivity without saturation limit is critical but challenging.

Here, we report a high-performance broadband photodiode that combines a special designed three-dimensional (3D) structure with a textured top ceiling electrode in combination with single-crystal nanowire arrays to maximize the absorption of near-infrared light and a conformal alumina layer inserted between the two constituent semiconductors of a p–n junction to form dual inversion layers. This structure design leads to significant enhancement of photoexcited charge separation and

carrier collection efficiency for both electrons and holes. The fabricated photodiodes are characterized by excellent sensitivity, fast response, and great stability working at low biasing voltage. Their photon response to light from near-ultraviolet (UV) to NIR is dramatically enhanced *via* the formed dual inversion layers and Fowler–Nordheim tunneling. Its sensitivity and responsivity drastically increase as the power intensity increases, and the saturation limit for silicon photodiodes is overcome. Overall, they meet the stringent requirements of optical-fiber communication systems, nanorobotics, analytical fields, biomedical sensing, and defense technology. To investigate how the insulator layer influences the transport of electrons and holes separately, we benefit from our specially designed device structure to only allow either electrons or holes to pass through the junction interfaces at a time by utilizing different wavelengths for excitation. We further apply the piezo-phototronic effect to modulate the charge density at the interface and to alter the energy bands and potential barrier distance of tunneling. This study would, therefore, help develop a better understanding of the p–insulator–n system and enable notable performance improvements in optoelectronics.

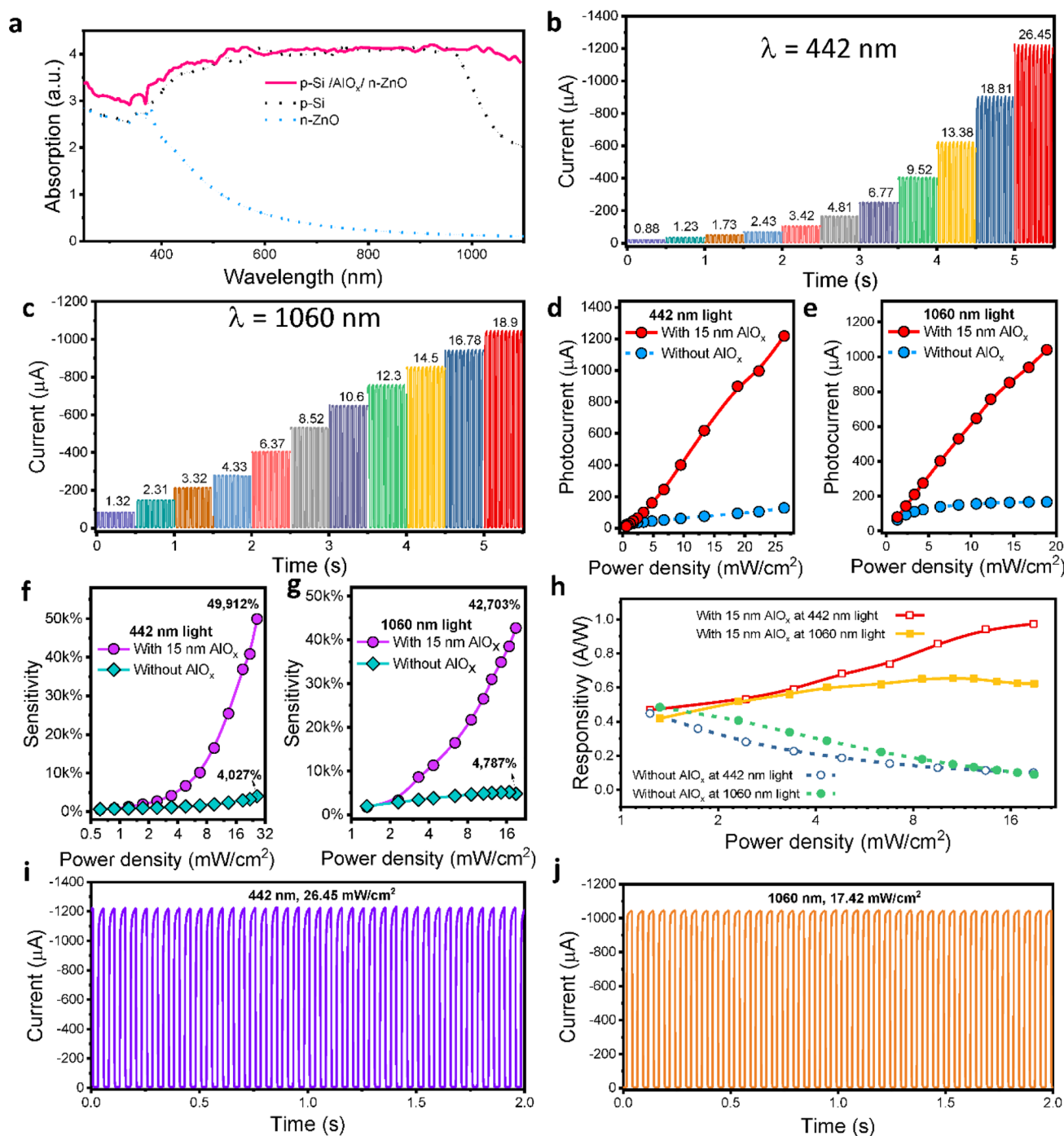


**Figure 2.** Optoelectronic characteristics of the photodetector. (a) Absorption spectra of p-Si, n-ZnO, and the p-Si/AlO<sub>x</sub>/n-ZnO devices. (b) Output current under different power densities of 442 nm light. (c) Output current under different power densities of 1060 nm light. Photocurrent of the device under illumination of 442 nm (d) and 1060 nm (e) with various power densities. The sensitivity of the devices under illumination power densities of 442 nm light (f) and 1060 nm light (g). (h) Responsivities of the devices under illumination power densities of 442 nm and 1060 nm light. Repeatability and time response of the device under 442 nm (i) and 1060 nm light (j). All measurements were performed at a reverse bias of  $-2$  V.

## RESULTS AND DISCUSSION

Figure 1a illustrates the schematic device structure of the broadband photodiode based on p-Si/AlO<sub>x</sub>/n-ZnO nanowire (NW) arrays. The device was fabricated by first coating the surface of the p-Si with a 15 nm thick atomic layer deposited (ALD) alumina (AlO<sub>x</sub>). Uniform ZnO NWs 70–80 nm in diameter and 2 μm in length were grown vertically on the AlO<sub>x</sub> layer.<sup>20,21</sup> A NIR antireflection layer of indium tin oxide (ITO)

top electrode was only developed at the tips of the NWs. The rear side of the wafer was coated with aluminum as the bottom electrode. Details of the fabrication methods are described in Experimental Section and Figure S1. The top view of the ZnO NWs is seen in the scanning electron microscope (SEM) image in Figure 1b, whereas the mushroom-like continuous ITO film is firmly supported by NWs and well contacted with the tips. Figure 1c shows the SEM image of a 30° tilt view of

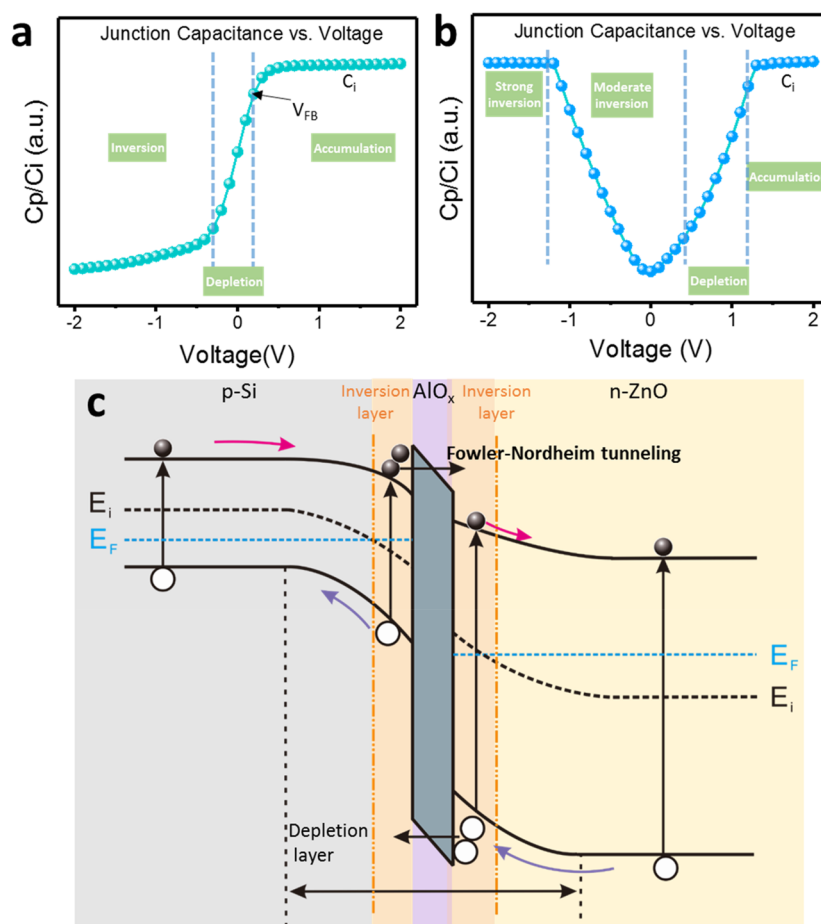


**Figure 3.** Principle of p-Si/AlO<sub>x</sub>/n-ZnO broadband photodetector. (a)  $C$ – $V$  characteristics of the p-Si/AlO<sub>x</sub>. For the device based on p-Si/AlO<sub>x</sub>/metal, the p-Si side was connected to the gate electrode of the measuring system.  $V_{FB}$  corresponds to the flat-band condition.  $C_i$  refers to the capacitance of the capacitor.  $C_p$  refers to the measured capacitance of the capacitor. (b)  $C$ – $V$  characteristics of the AlO<sub>x</sub>/n-ZnO NW arrays. The n-ZnO side for the device based on metal/AlO<sub>x</sub>/n-ZnO NW arrays was grounded, while the metal side was connected to the gate electrode of the measuring system. (c) Energy-band diagram in p–insulator–n for the dual inversion layers mode under an appropriate large negative bias. The charge carrier flow through the insulating layer is by quantum mechanical Fowler–Nordheim tunneling. Two inversion layers are formed at the two sides of the insulating layer. The conduction and valence band edges bend as shown in the figure, indicating a space charge region similar to that in a pn junction. The conduction band and intrinsic Fermi levels move closer to the Fermi level. The intrinsic Fermi level  $E_i$  at the surface is now below the Fermi level  $E_F$ ; thus, the surface of the semiconductor adjacent to the oxide–semiconductor interface has been inverted from a p-type to an n-type semiconductor. Similarly, an inversion layer is generated at the interface of oxide/n-ZnO nanowire arrays.

the device at the edge. Hence, the ITO electrode has a textured structure with a mushroom-like top surface and a flat bottom surface. The suspended top ceiling electrode could avoid current leakage and short-circuit of the NWs. The transmission electron microscopy (TEM) image in Figure 1d shows the cross-section of the p–insulator–n structure, where the AlO<sub>x</sub> layer is found to be 14.5 nm. The energy dispersive X-ray spectroscopy (EDS) spectrum profile image and data (Figure 1e,f) show the elementary distribution from which the full width at half-maximum (fwhm) of the Al peak can also yield the thickness of the AlO<sub>x</sub> layer. The vertical growth of strongly oriented ZnO NWs is confirmed by means of X-ray diffraction in Figure 1g. The elementary analysis from the EDS data across the junctions is shown in Figure 1h.

Absorption spectra of the device are shown in Figure 2a. The absorption of light over a 950 nm wavelength is significantly improved in comparison with a planar silicon. A thin layer of AlO<sub>x</sub> does not contribute to improving the absorption, as the transmittance of a ~15 nm AlO<sub>x</sub> layer is nearly 100%, as shown in Figure S2. The improved light absorption is attributed to the

antireflection layer of the ITO top electrode, as the textured top layer is effective in reducing the reflection of incident light and the flat bottom layer returns the reflected light to the absorbing materials. A typical  $I$ – $V$  curve of the photodiode is shown in Figure S3. It is worth noting that at the period of negative bias there is a hysteresis loop: the current is larger in absolute value when the applied voltage is increased than that when it is decreased. This is different from the p–n junction, and further studies are required to understand the possible theoretical principles. The p-Si/AlO<sub>x</sub>/n-ZnO NW array broadband photodetectors are found to exhibit good photo-sensing properties at a bias voltage as low as –2 V. The current output curves under various illumination intensities at 442 and 1060 nm are shown in Figure 2b and c, respectively. The rise time is defined as the time interval for the response to rise from 10% to 90% of its peak value, and the fall time is defined as the time interval for the response to decay from 90% to 10% of its peak value. From Figure S4, the rise time is as short as 260 μs, and the fall time could even reach 220 μs, which demonstrates

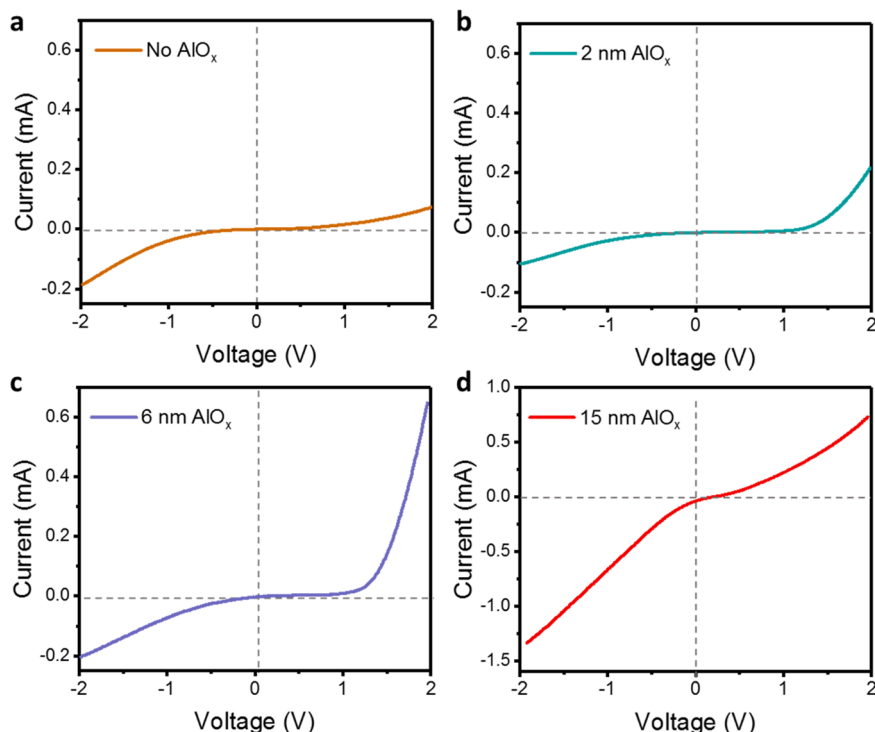


**Figure 4.** Current–voltage ( $I$ – $V$ ) characteristic of the photodetector under 442 nm light with  $26.45 \text{ mW/cm}^2$  for various thicknesses of  $\text{AlO}_x$  between the p–n junctions. The thicknesses of 2 and 6 nm that allow the direct tunneling do not promote the charge separations.

that this device is suitable for photodetection applications that are operated at high-speed response conditions.

The performance of the p–insulator–n junction device is compared with its counterpart without the  $\text{AlO}_x$  insulator layer. The photocurrent ( $|I| = |I_{\text{light}} - I_{\text{dark}}|$ ) for the device with  $\text{AlO}_x$  is more than 9.5 times larger under the illumination at 442 nm and with the intensity of  $26.45 \text{ mW/cm}^2$  (Figure 2d) and about 6.2 times larger at 1060 nm and with the intensity of  $18.9 \text{ mW/cm}^2$  (Figure 2e). Under illumination at 1060 nm, the reference device without  $\text{AlO}_x$  displays a saturation limit with no additional photocurrent when the incident optical power increases above  $15 \text{ mW/cm}^2$  (Figure S6). In contrast, the p–insulator–n device demonstrates a linear increase of the photocurrent with the incident light power in the studied range, which overcomes the limitation. The sensitivity, which is defined as  $(I_{\text{light}} - I_{\text{dark}})/I_{\text{dark}}$ , reaches about 50 900% at 442 nm light and 42 700% at 1060 nm light. The sensitivity of the p–insulator–n device is 12.4 and 8.9 times larger than that of the reference device under illumination at 442 nm (Figure 2f) and 1060 nm (Figure 2g), respectively. The results demonstrate that the carrier separation has been greatly improved in the p–insulator–n junction. The responsivity of the photodetector,  $R$ , is defined as

$$R = \frac{I_{\text{light}} - I_{\text{dark}}}{P_{\text{ill}}} = \frac{\eta_{\text{ext}} \Gamma_{\text{G}}}{h\nu}$$

where  $P_{\text{ill}} = I_{\text{ill}} \times S$  is the illumination power on the photodiode;  $I_{\text{light}}$  and  $I_{\text{dark}}$  represent the photo and dark current, respectively;  $\Gamma_{\text{G}}$  is the internal gain;  $\eta_{\text{ext}}$  is the external quantum efficiency (EQE);  $h$  is Planck's constant;  $\nu$  is the frequency of the light;  $I_{\text{ill}}$  is the excitation power density;  $S$  is the effective area of the photodiode. The variation of  $R$  with power density of the incident light is shown in Figure 2h. The responsivity reached  $\sim 1 \text{ A/W}$  at 442 nm with  $17.42 \text{ mW/cm}^2$ ,

which is more than 5 times over the performance of commercial silicon photodiodes (FDS1010 from Thorlabs, Si PIN photodiode from Hamamatsu<sup>22</sup>). At 1060 nm light with  $12.3 \text{ mW/cm}^2$ , the responsivity reached  $\sim 0.65 \text{ A/W}$ , which is also significantly higher than the commercial silicon photodiodes (by comparing with FDS1010 from Thorlabs, Si photodiode S12497 from Hamamatsu, and IR-enhanced Si PIN photodiode<sup>23</sup>). As expected,<sup>24–27</sup> the responsivity of the reference photodetector without  $\text{AlO}_x$  decreases with increasing light power density. Contrarily, however, the responsivity of the p–insulator–n photodetector continuously increases with increasing light power density. This observation may be interpreted as follows. The Fermi levels and bands shift as the intensity of light is increased, leading to more oppositely charged carriers appearing in the inversion layers at the semiconductor–oxide interfaces. Thus, stronger inversion layers of opposite polarity would be expected,<sup>8</sup> resulting in higher current-collection capability.<sup>28</sup> Stability and repeatability of light responses at 442 nm with  $28.46 \text{ mW/cm}^2$  and 1060 nm light with  $17.42 \text{ mW/cm}^2$  are shown in the current–time curves in Figure 2i and j, respectively. Consequently, this broadband photodetector based on the p-Si/i- $\text{AlO}_x$ /n-ZnO-NW heterojunction exhibits significant improvements in its photosensing properties over conventional photodiodes, not only in the visible but also in the NIR region. It operates with low power consumption and is characterized by high sensitivity, high responsivity, fast response, great linearity without saturation limit, and excellent stability.

To study the key role of the middle ALD alumina layer in carrier transport during broadband detection, capacitance–voltage ( $C$ – $V$ ) characteristics were measured to confirm the presence of inversion layers in the device structure. Two devices based on these two separate junctions of p-Si/ $\text{AlO}_x$  and  $\text{AlO}_x$ /n-ZnO were fabricated. The  $C$ – $V$  measurements

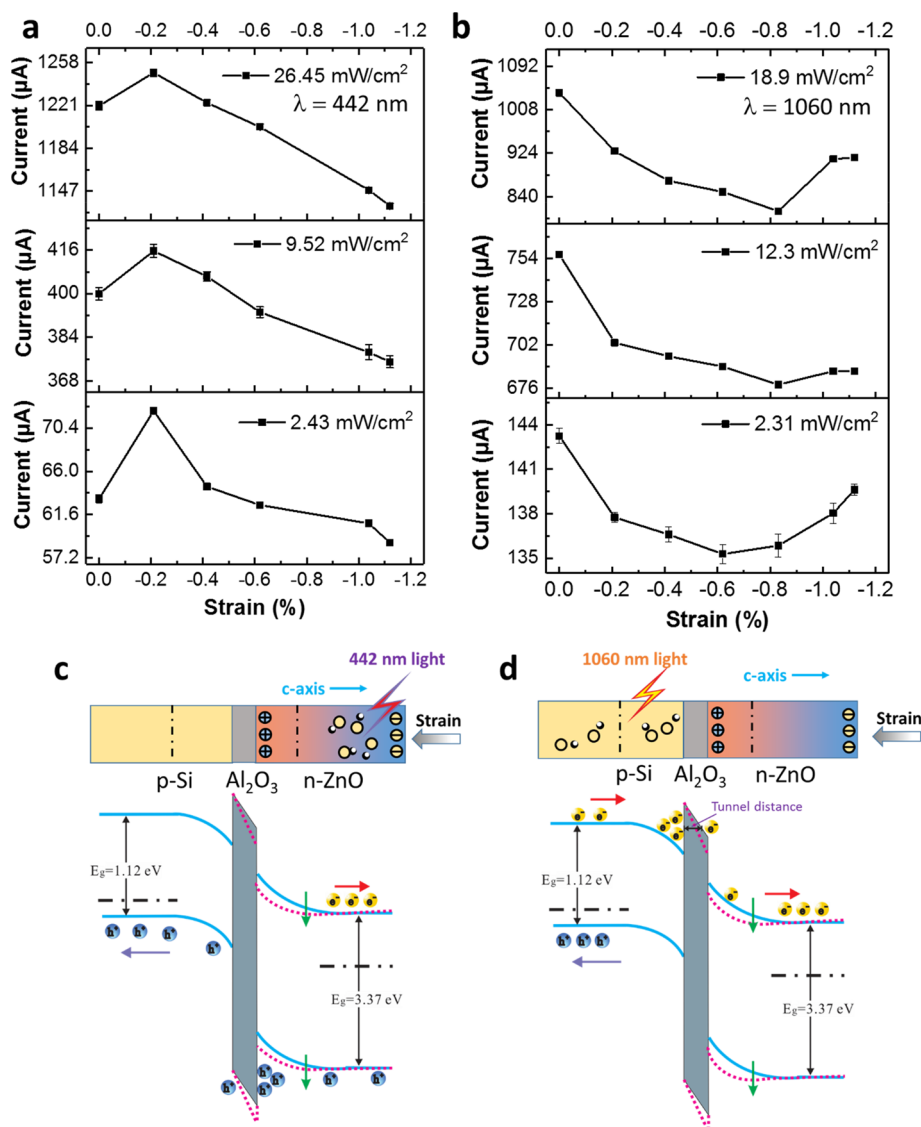


**Figure 5.** Study of the effect of  $\text{AlO}_x$  on electron and hole transport by using the piezo-phototronic effect. Current output under different strains at  $-2$  V bias voltage under illumination at 442 nm (a) and 1060 nm (b) with different power densities. Band diagrams of the broadband photodiode at negative bias at 442 nm light (c) and 1060 nm light (d). At 442 nm, the  $\sim 2$   $\mu\text{m}$  thickness of n-ZnO absorbs most of the light, and the photoexcited carriers are generated only on the n-ZnO side. Similarly, at 1060 nm, p-Si absorbs most of the light, and the photoexcited carriers are generated only on the p-Si side. For the color gradient, pink represents positive piezo-charges and blue represents negative piezo-charges. The blue lines are the energy bands at the initial stage without strain, and the short dotted lines are the energy bands when external strain is applied.

shown in Figure 3a,b were carried out on the two devices in the dark, ranging from  $-2$  to  $2$  V at 1 MHz. For the p-Si/ $\text{AlO}_x$ /metal device, the p-Si side was connected to the gate electrode of the measuring system, while the metal side was grounded. When the gate voltage was swept from positive to negative, the device state with respect to carrier type in the p-Si at the Si/ $\text{AlO}_x$  interface would change from accumulation (of holes), to depletion, and to inversion (with electrons). When a sufficiently large negative gate voltage was applied, the bands near the interface bent downward to such an extent that the intrinsic Fermi level  $E_i$  would lie below the Fermi level  $E_F$  (shown as the left side of the insulator layer in Figure 3c and Figure S7a). At this point, the semiconductor surface adjacent to the oxide–semiconductor interface was inverted from p-type to n-type. For the metal/ $\text{AlO}_x$ /n-ZnO NW array device, the metal side was connected to the gate electrode of the

measuring system, while the n-ZnO NW arrays were grounded. When the gate voltage was swept from positive to negative, the state changed from accumulation, to depletion, to moderate inversion, and to strong inversion (Figure 3b). The different appearance of the  $C-V$  curves of the two devices is due to the measuring frequency 1 MHz being too high for the silicon substrate to generate minority carriers (electrons), but apparently posing little demand on ZnO NWs for generation of minority carriers (holes).<sup>29</sup> This result implies that the semiconductor surface adjacent to the oxide–semiconductor interface was inverted from n-type to p-type (shown as the right side of the insulator layer in Figure 3c and Figure S7b). From the results, when a sufficient reverse bias is applied to the two sides of the p-insulator–n heterojunction, two inversion layers would be simultaneously induced at the respective oxide–semiconductor interfaces. Figure 3c shows the

schematic energy-band diagram of the p-insulator–n structure wherein the formation of the dual inversion layers is highlighted. Clearly, the device of p-Si/ $\text{AlO}_x$ /n-ZnO NW arrays offers efficient charge carrier separation and a high carrier collection efficiency. The inversion layers of opposite polarity would build up a strong electric field across the insulator layer,<sup>28</sup> which would sweep the photoexcited carriers out of the p and n regions to be collected by electrodes. There is another possible reason: with the passivation of  $\text{AlO}_x$ , the surface dangling bonds could be efficiently reduced, and the surface recombination is then suppressed.<sup>28</sup> But this is not the main reason. Different thicknesses of alumina (0–15 nm) deposited by ALD are introduced in the fabricated devices. The results demonstrate that the direct tunneling *via* the ultrathin alumina does not enhance the charge separation much (Figure 4). Therefore, an appropriate thickness of alumina is required to form the dual inversion layers and to allow the Fowler–Nordheim tunneling rather than the direct tunneling.

Ideally, the conductance of  $\text{AlO}_x$  is considered to be zero. However, real insulators with thin thickness show some degree of carrier conduction when the electric field is sufficiently high. Quantum mechanical tunneling describes the transition of carriers through a classically forbidden energy state. It is a result of quantum mechanics by which the electron wave function can penetrate through a potential barrier, even if the energy barrier is higher than the electron energy. Direct tunneling usually works for ultrathin insulators, but a 15 nm thick  $\text{AlO}_x$  is unlikely for electrons to directly tunnel through. The Fowler–Nordheim regime is significant for thicker dielectrics and sufficiently high electric fields. Under the applied voltage, the energy bands bend downward, leading to a constant thinning of the effective dielectrics owing to an inclined band at the junction region. Consequently, carriers can tunnel through such a “thinned oxide” especially at its tip/bottom, where they encounter only a partial width of the barrier; thus the effect of tunneling drastically gains relevance. As shown in Figure 3c, the carriers tunnel from the inversion layer to the energy bands at the other side.

To better understand the effect of the insulator layer on the transport of electrons and holes separately, the piezo-phototronic effect was employed to modify the charge density at the interface between oxide and semiconductor by applying mechanical strains to induce the piezo-charges. In this way, we are able to shift the energy bands and even alter potential barrier width for tunneling in the same device without the need to change the materials. The piezo-phototronic effect is the use of the piezo-potential to tune/control the optoelectronic processes at an interface/junction.<sup>30,31</sup> In a non-centrosymmetric wurtzite semiconducting crystal, the piezoelectric charges would be induced at the interface between the ZnO NWs and the insulator due to dipole moments caused by mechanical strains. In the depletion region, the induced positive charges by compression would be mostly preserved without being screened by local residual free carriers in the majority carrier-free zone. This would shift the energy bands of ZnO NWs as well as those of the insulator, and the effective thickness for tunneling would be adjusted consequently. We can also selectively choose the photogenerated charge carriers (either electrons or holes) passing through the interfaces, by using illumination of different wavelengths of light. Under an illumination of 442 nm, ~95.3% of light was absorbed by the ZnO NWs (Figure S8), leading to the generation of electron–

hole pairs in the ZnO NW arrays. The electrons were directly collected by the electrode, while the holes went across the interfaces. Similarly, under an illumination of 1060 nm, electron–hole pairs were generated only in the silicon substrate, and furthermore only the electrons would pass through the insulator layer. This distinction enables the possibility to investigate separately how the electrons and holes respond to the band shift with the presence of an insulator layer between the p- and n-regions and how the inversion layers and tunneling influence the output photocurrent when the barrier width of tunneling is altered.

The experimental setup to apply the piezo-phototronic effect is shown in Figure S9. Figure 5a shows that when an external compressive strain is applied, the photocurrent under various illumination intensities at 442 nm increases first and then decreases. At 1060 nm in Figure 5b, the photocurrent shows different behaviors; it falls continuously and then increases at very high strains. The distinct trends of photocurrent demonstrate that the transfer of electrons and holes across the  $\text{AlO}_x$  layer behaves differently. Since the ZnO NW arrays were grown vertically on the surface of silicon, a compressive strain would induce positive piezoelectric charges at the interface of  $\text{AlO}_x$ /n-ZnO NW arrays (Figure 5c). At 442 nm, the positive piezo-charges would be added to the inversion layer on the ZnO NW array side and thereby increase the charge density there, which would build up a stronger internal electric field, so the charge separation and collection would become more efficient. When the strain was further increased, the piezo-potential would tend to bend down the local bands of n-ZnO slightly, as well as the bands of  $\text{AlO}_x$ . Further pulling down the band at one side relative to the opposite side of the  $\text{AlO}_x$  layer would change the charge density accumulated at the interface (Figure 3c). As a result, the charge separation and collection efficiency would be slightly compromised. At 1060 nm, when a compressive strain is applied to the ZnO NWs, the bands of the  $\text{AlO}_x$  layer would be bent downward due to the strain-induced positive piezo-charges at the interface and the tunnel distance for tunneling would be reduced. Then, the charge density accumulated at the interface on the p-Si side would be lower, and the inversion layer would become weaker so that the photocurrent would be decreased. As the strain is further increased, the decreased tunneling distance would be small enough for the carriers to move across the insulator layer directly without accumulating charge to form a strong inversion layer. As a decreased photocurrent would result in a weakened screening effect on the piezo-charges, the piezo-phototronic effect turns out to be more significant, leading to an increase of the photocurrent as a conventional p–n junction.<sup>27,32,33</sup>

## CONCLUSIONS

In conclusion, we have fabricated an ultra-high-performance broadband photodetector with enhanced absorption and carrier collection based on the heterojunction of p-Si/ $\text{AlO}_x$ /n-ZnO NW arrays working over a wide wavelength range from 442 to 1060 nm. The specially designed ITO top electrode greatly improved the absorption of near-infrared light above 900 nm, thereby overcoming the material limitation of silicon. The top ceiling electrode avoids the short-circuit of nanowires when the ITO was directly deposited on the top, so that the light response of the device would benefit from the features of the high-quality single-crystal nanowires. By introducing a ~15 nm thick  $\text{AlO}_x$  dielectric layer in the conventional p–n

junction, the performance of light detection was dramatically enhanced. Different from conventional photodiodes, the responsivity of the heterojunction diode device increases sharply when the intensity of incident light increases, which overcomes the issue of saturation limit for other conventional devices. Dual inversion layers were formed at the two sides of the insulator layer under the operating conditions. The barrier function of the  $\text{AlO}_x$  insulator led to an excessively high carrier concentration in the inversion layers; thus a high collection efficiency was achieved. Additionally, the fabrication process is compatible with the existing semiconductor processing techniques at low temperature *via* a dopant-free method. The piezo-phototronic effect was exploited to study in-depth the mechanism and the effect of an insulator layer on carrier transport. By exploiting the piezoelectric property of ZnO NWs, piezo-charges were induced by mechanical strain to modulate the energy bands and alter the tunneling distance. In combination with utilizing different wavelengths of light, the experimental observations demonstrated helped understand the implications of the  $\text{AlO}_x$  insulator layer in the transport of electrons and/or holes separately, as well as served as guidelines for the design of high-performance photodetection devices. Given the obtained results, the fabricated devices presented in this work would potentially render a practical and effective approach to converting light to electricity efficiently, and therefore to achieve better performance for optoelectronics.

## EXPERIMENTAL SECTION

### Fabrication Process of the p-Si/ $\text{Al}_2\text{O}_3$ /n-ZnO Photodetector.

Each device had a size of 1 cm  $\times$  1 cm sliced from a p-type Si wafer (100 mm, B-doped, 1–10  $\Omega$ -cm resistivity, (100) orientation, 500  $\mu\text{m}$  thickness, from UniversityWafer Inc.) which was washed in an ultrasonicator with acetone, isopropyl alcohol, and distilled water each for 20 min. An  $\text{AlO}_x$  layer of 15 nm thickness was coated on the samples in a Cambridge NanoTech Plasma ALD chamber. A ZnO seed layer was deposited by RF magnetron sputtering (PVD RF75, Kurt J. Lesker Company) with a thickness of about 100 nm. The coated p-Si wafer was then placed into a mixed growth solution (25 mM  $\text{Zn}(\text{NO}_3)_2$ , 12.5 mM hexamethylenetetramine, and 0.8 M ammonium hydroxide) in a mechanical convection oven (Yamato DKN400, Santa Clara, CA, USA) at 95  $^\circ\text{C}$  for 90 min. The samples were subsequently washed with isopropyl alcohol and distilled water and dried in the oven at 60  $^\circ\text{C}$  for an hour. Poly(methyl methacrylate) (PMMA, MicroChem 495PMMA A8) was spin-coated onto the samples, and then the samples were treated with oxygen plasma in a Vision RIE for 4 min to expose the tips of the ZnO nanowires. A thin layer of ITO was deposited on ZnO as the top electrode, and Al was deposited on the rear side of the p-Si wafer as the bottom electrode. The samples were then cleaned by acetone to remove the PMMA layer and annealed at 350  $^\circ\text{C}$  for 2 h in a compact rapid thermal processing tube furnace (RTP-1000D4, MTI Corporation). Testing wires were connected to the electrodes by silver paste.

The devices based on p-Si/ $\text{AlO}_x$ /metal were fabricated following the same procedure described above, where an aluminum layer was deposited at the rear side of p-Si as the back electrode and the ITO was deposited at the surface of  $\text{AlO}_x$ . For the devices based on metal/ $\text{AlO}_x$ /n-ZnO NW arrays, the  $\text{AlO}_x$  was deposited on a  $\text{p}^{+2}$ -Si substrate (Universitywafer, Inc., 0.001–0.005 ohm.cm) that was subsequently used as the conductive electrode (*i.e.*, metal). The suspended top ceiling ITO antireflection electrode was deposited in the same way as described above.

**Material Characterizations.** Detailed microscopic structures of ZnO NWs were characterized by scanning electron microscope (Hitachi SU 8010).

**Measurements.** A piece of sapphire was fixed on the sample holder by layers of double-adhesive Kapton tape. The sample was then settled on the sapphire by the Kapton tape. External strains were applied onto the sample by pressing the surface of the device through another piece of sapphire (Figure S9) with a 3D mechanical stage (movement resolution  $\approx$  10  $\mu\text{m}$ ). The device was fixed onto the stage through double-sided Kapton polyimide tape. Transmission and absorption spectra of materials were measured by a UV–vis spectrophotometer (JASCO V-630).

Current *versus* voltage ( $I$ – $V$ ) characteristics of the devices were measured and recorded by a computer-controlled measurement system with a Stanford SRS low-noise current preamplifier (SR570)/SRS low-noise voltage preamplifier (SR560) in conjunction with a GPIB controller (GPIB-USB-HS, NI 488.2). The optical input stimuli were provided by a He–Cd laser (wavelength = 442 nm, model no. KI5751I-G, Kimmon Koha Co., Ltd.). A continuously variable filter was used to control the light power density, which was measured by a thermopile power meter (Newport 818P-001-12). The capacitance *versus* voltage ( $C$ – $V$ ) measurements were carried out with a Keithley 4200 at 1 MHz.

## ASSOCIATED CONTENT

### Supporting Information

The Supporting Information is available free of charge on the ACS Publications website at DOI: 10.1021/acsnano.8b08998.

Processing scheme, transmittance spectra, current–voltage characteristics, response time, stability in a long time range, saturation limit for p–n junctions, schematic energy band diagram,  $I$ – $V$  characteristics with various thicknesses of  $\text{AlO}_x$ , absorption spectra, and experiment setup (PDF)

## AUTHOR INFORMATION

### Corresponding Authors

\*E-mail: Shili.Zhang@angstrom.uu.se.

\*E-mail: zhong.wang@mse.gatech.edu.

### ORCID

Haiyang Zou: 0000-0003-3927-8651

Xiaogan Li: 0000-0003-4257-8380

Guozhang Dai: 0000-0003-3821-7099

Wenbo Peng: 0000-0003-4917-6851

Shi-Li Zhang: 0000-0003-2417-274X

Zhong Lin Wang: 0000-0002-5530-0380

### Author Contributions

Z.L.W. supervised and guided the project; H.Z. conceived and designed the study; H.Z., X.L., and G.D. fabricated the devices; H.Z., X.L., Z.Y., A.C.W., S.Z., and X.C. performed the experiments; D.Y. did the TEM work; Z.L.W., H.Z., and S.L.Z. analyzed the data; H.Z., X.L., G.D., Y.Z., S.L.Z., and Z.L.W. prepared the manuscript with input from all authors.

### Notes

The authors declare no competing financial interest.

## ACKNOWLEDGMENTS

This research was supported by U.S. Department of Energy, Office of Basic Energy Sciences (Award DE-FG02-07ER46394), and the Hightower Chair Foundation.

## REFERENCES

- (1) Thomson, D.; Zilkie, A.; Bowers, J. E.; Komljenovic, T.; Reed, G. T.; Vivien, L.; Marris-Morini, D.; Cassan, E.; Viro, L.; Fédéli, J.-M. Roadmap on Silicon Photonics. *J. Opt.* **2016**, *18*, No. 073003.

- (2) Hochberg, M.; Baehr-Jones, T. Towards Fabless Silicon Photonics. *Nat. Photonics* **2010**, *4*, 492–494.
- (3) Atabaki, A. H.; Moazeni, S.; Pavanello, F.; Gevorgyan, H.; Notaros, J.; Alloatti, L.; Wade, M. T.; Sun, C.; Kruger, S. A.; Meng, H.; Al Qubaisi, K.; Wang, I.; Zhang, B.; Khilo, A.; Baiocco, C. V.; Popovic, M. A.; Stojanovic, V. M.; Ram, R. J. Integrating Photonics with Silicon Nanoelectronics for the Next Generation of Systems on a Chip. *Nature* **2018**, *556*, 349–354.
- (4) Asghari, M.; Krishnamoorthy, A. V. Photonics Silicon Energy-Efficient Communication. *Nat. Photonics* **2011**, *5*, 268–270.
- (5) Leuthold, J.; Koos, C.; Freude, W. Nonlinear Silicon Photonics. *Nat. Photonics* **2010**, *4*, 535–544.
- (6) Liu, Y.; Das, A.; Lin, Z. Y.; Cooper, I. B.; Rohatgi, A.; Wong, C. P. Hierarchical Robust Textured Structures for Large Scale Self-Cleaning Black Silicon Solar Cells. *Nano Energy* **2014**, *3*, 127–133.
- (7) Priolo, F.; Gregorkiewicz, T.; Galli, M.; Krauss, T. F. Silicon Nanostructures for Photonics and Photovoltaics. *Nat. Nanotechnol.* **2014**, *9*, 19–32.
- (8) Ccama, A. G. Photodetectors; <https://www.slideshare.net/rathur/chap6-photodetectors> (accessed Oct 12, 2018).
- (9) Zou, H.; Li, X.; Peng, W.; Wu, W.; Yu, R.; Wu, C.; Ding, W.; Hu, F.; Liu, R.; Zi, Y.; Wang, Z. L. Piezo-Phototronic Effect on Selective Electron or Hole Transport through Depletion Region of Vis-Nir Broadband Photodiode. *Adv. Mater.* **2017**, *29*, 1701412.
- (10) Quimby, R. S. *Photonics and Lasers: An Introduction*; John Wiley & Sons: Hoboken, 2006; pp 223–236.
- (11) Buscema, M.; Island, J. O.; Groenendijk, D. J.; Blanter, S. I.; Steele, G. A.; van der Zant, H. S. J.; Castellanos-Gomez, A. Photocurrent Generation with Two-Dimensional Van Der Waals Semiconductors. *Chem. Soc. Rev.* **2015**, *44*, 3691–3718.
- (12) Green, M. A. *Solar Cells: Operating Principles, Technology, and System Applications*; Prentice-Hall: Englewood Cliffs, 1982; pp 50–80.
- (13) Mukherjee, S.; Das, K.; Kakati, A.; Soumen, D.; Ray, S. K.; Raychaudhuri, A. K. Single Silicon Nanowire Based Broadband Photodetector with Superior Responsivity. *International Conference on Fibre Optics and Photonics, Optical Society of America* **2014**, T3A. 69.
- (14) Juntunen, M. A.; Heinonen, J.; Vahanissi, V.; Repo, P.; Valluru, D.; Savin, H. Near-Unity Quantum Efficiency of Broadband Black Silicon Photodiodes with an Induced Junction. *Nat. Photonics* **2016**, *10*, 777.
- (15) Spinelli, P.; Verschuuren, M. A.; Polman, A. Broadband Omnidirectional Antireflection Coating Based on Subwavelength Surface Mie Resonators. *Nat. Commun.* **2012**, *3*, 692.
- (16) Kuo, M. L.; Poxson, D. J.; Kim, Y. S.; Mont, F. W.; Kim, L. K.; Schuhert, E. F.; Lin, S. Y. Realization of a near-Perfect Antireflection Coating for Silicon Solar Energy Utilization. *Opt. Lett.* **2008**, *33*, 2527–2529.
- (17) Shi, E. Z.; Li, H. B.; Yang, L.; Zhang, L. H.; Li, Z.; Li, P. X.; Shang, Y. Y.; Wu, S. T.; Li, X. M.; Wei, J. Q.; Wang, K. L.; Zhu, H. W.; Wu, D. H.; Fang, Y.; Cao, A. Y. Colloidal Antireflection Coating Improves Graphene-Silicon Solar Cells. *Nano Lett.* **2013**, *13*, 1776–1781.
- (18) Nagel, H.; Aberle, A. G.; Hezel, R. Optimised Antireflection Coatings for Planar Silicon Solar Cells Using Remote Pevd Silicon Nitride and Porous Silicon Dioxide. *Prog. Photovoltaics* **1999**, *7*, 245–260.
- (19) Michel, J.; Liu, J. F.; Kimerling, L. C. High-Performance Ge-on-Si Photodetectors. *Nat. Photonics* **2010**, *4*, 527–534.
- (20) Pradel, K. C.; Wu, W. Z.; Zhou, Y. S.; Wen, X. N.; Ding, Y.; Wang, Z. L. Piezotronic Effect in Solution-Grown P-Type ZnO Nanowires and Films. *Nano Lett.* **2013**, *13*, 2647–2653.
- (21) Pradel, K. C.; Wu, W. Z.; Ding, Y.; Wang, Z. L. Solution-Derived ZnO Homo Junction Nanowire Films on Wearable Substrates for Energy Conversion and Self-Powered Gesture Recognition. *Nano Lett.* **2014**, *14*, 6897–6905.
- (22) Thorlabs Photodiodes; [https://www.thorlabs.com/newgrouppage9.cfm?objectgroup\\_id=285&pn=FDS1010#](https://www.thorlabs.com/newgrouppage9.cfm?objectgroup_id=285&pn=FDS1010#) (accessed Oct 10, 2018).
- (23) Si Photodiode; <https://www.hamamatsu.com/us/en/product/type/S12497/index.html> (accessed Oct 10, 2018).
- (24) Lopez-Sanchez, O.; Lembke, D.; Kayci, M.; Radenovic, A.; Kis, A. Ultrasensitive Photodetectors Based on Monolayer Mos<sub>2</sub>. *Nat. Nanotechnol.* **2013**, *8*, 497–501.
- (25) Konstantatos, G.; Clifford, J.; Levina, L.; Sargent, E. H. Sensitive Solution-Processed Visible-Wavelength Photodetectors. *Nat. Photonics* **2007**, *1*, 531–534.
- (26) Liu, Y. D.; Wang, F. Q.; Wang, X. M.; Wang, X. Z.; Flahaut, E.; Liu, X. L.; Li, Y.; Wang, X. R.; Xu, Y. B.; Shi, Y.; Zhang, R. Planar Carbon Nanotube-Graphene Hybrid Films for High-Performance Broadband Photodetectors. *Nat. Commun.* **2015**, *6*, 8589.
- (27) Dai, G. Z.; Zou, H. Y.; Wang, X. F.; Zhou, Y. K.; Wang, P. H.; Ding, Y.; Zhang, Y.; Yang, J. L.; Wang, Z. L. Piezo-Phototronic Effect Enhanced Responsivity of Photon Sensor Based on Composition-Tunable Ternary Cds<sub>x</sub>Se<sub>1-x</sub> Nanowires. *ACS Photonics* **2017**, *4*, 2495–2503.
- (28) Sun, T.; Wang, R. B.; Liu, R. Y.; Wu, C.; Zhong, Y. N.; Liu, Y. Q.; Wang, Y. S.; Han, Y. J.; Xia, Z. H.; Zou, Y. T.; Song, T.; Koch, N.; Duhm, S.; Sun, B. Q. Investigation of Moox/N-Si Strong Inversion Layer Interfaces Via Dopant-Free Heterocontact. *Phys. Status Solidi RRL* **2017**, *11*, 1700107.
- (29) Sze, S. M.; Ng, K. K. *Physics of Semiconductor Devices*; John Wiley & Sons: Hoboken, 2006; pp 197–238.
- (30) Liu, Y.; Zhang, Y.; Yang, Q.; Niu, S. M.; Wang, Z. L. Fundamental Theories of Piezotronics and Piezo-Phototronics. *Nano Energy* **2015**, *14*, 257–275.
- (31) Wang, Z. L.; Wu, W. Z. Piezotronics and Piezo-Phototronics: Fundamentals and Applications. *Natl. Sci. Rev.* **2014**, *1*, 62–90.
- (32) Yang, Q.; Guo, X.; Wang, W. H.; Zhang, Y.; Xu, S.; Lien, D. H.; Wang, Z. L. Enhancing Sensitivity of a Single ZnO Micro-/Nanowire Photodetector by Piezo-Phototronic Effect. *ACS Nano* **2010**, *4*, 6285–6291.
- (33) Wang, Z. N.; Yu, R. M.; Pan, C. F.; Liu, Y.; Ding, Y.; Wang, Z. L. Piezo-Phototronic Uv/Visible Photosensing with Optical-Fiber-Nanowire Hybridized Structures. *Adv. Mater.* **2015**, *27*, 1553–1560.